Inorg. Chem. **2004**, *43*, 4216–4226

Amphiphilic Ruthenium Sensitizers and Their Applications in Dye-Sensitized Solar Cells

C. Klein, Md. K. Nazeeruddin,* D. Di Censo, P. Liska, and Michael Grätzel*

Laboratory for Photonics and Interfaces, Institute of Chemical Sciences and Engineering, Swiss Federal Institute of Technology, CH-1015 Lausanne, Switzerland

Received January 23, 2004

Amphiphilic ligands 4,4′-bis(1-adamantyl-aminocarbonyl)-2,2′-bipyridine (**L**[1]), 4,4′-bis{5-{*N*-[2-(3β-cholest-5-en-3-ylcarbamate-*N*-yl)ethyl]aminocarbonyl}}-2,2′-bipyridine (**L**[2]), 4,4′-bis{5-{*N*-[2-(3β-cholest-5-en-3-ylcarbamate-*N*-yl)-propyl]aminocarbonyl}}-2,2′-bipyridine (**L**[3]), and 4,4′-bis(dodecan-12-ol)-2,2′-bipyridine (**L**[4]) and their heteroleptic ruthenium(II) complexes of the type [Ru(II)LL[1](NCS)$_2$] (**5**), [Ru(II)LL[2](NCS)$_2$] (**6**), [Ru(II)LL[3](NCS)$_2$] (**7**), and [Ru(II)-LL[4](NCS)$_2$] (**8**) (where L = 4,4′-bis(carboxylic acid)-2,2′-bipyridine) have been synthesized starting from dichloro-(p-cymene)ruthenium(II) dimer. All the ligands and the complexes were characterized by analytical, spectroscopic, and electrochemical techniques. The performance of these complexes as charge-transfer photosensitizers in nanocrystalline TiO_2-based solar cells was studied. When complexes **5**–**8** anchored onto a 12 + 4 μm thick nanocrystalline TiO_2 films, very efficient sensitization was achieved (85 ± 5% incident photon-to-current efficiencies in the visible region, using an electrolyte consisting of 0.6 M butylmethylimidazolium iodide, 0.05 M I_2, 0.1 M LiI, and 0.5 M *tert*-butyl pyridine in 1:1 acetonitrile + valeronitrile). Under standard AM 1.5 sunlight, the complex **8** yielded a short-circuit photocurrent density of 17 ± 0.5 mA/cm^2, the open-circuit voltage was 720 ± 50 mV, and the fill factor was 0.72 ± 0.05, corresponding to an overall conversion efficiency of 8.8 ± 0.5%.

1. Introduction

Dye-sensitized solar cells are currently attracting widespread academic and commercial interest for the conversion of sunlight into electricity because of their low cost and high efficiency. Over the past few years, considerable progress has been made in understanding the function of various components of dye-sensitized solar cells.[1−20] A schematic representation of operating principles and an energy level diagram of a dye-sensitized solar cell is shown in Figure 1. In these cells, several ruthenium complexes containing anchoring groups such as carboxylic acid, dihydroxy, and phosphonic acid on pyridyl ligands have been used as dyes.[21−23] The anchoring groups serve to immobilize the dye

* Authors to whom correspondence should be addressed. E-mail: MdKhaja.Nazeeruddin@epfl.ch (M.K.N.).

(1) Nazeeruddin, M. K.; Kay, A.; Rodicio, I.; Humphry-Baker, R.; Muller, E.; Liska, P.; Vlachopoulos, N.; Grätzel, M. *J. Am. Chem. Soc.* **1993**, *115*, 6382.
(2) Wang, P.; Zakeeruddin, S. M.; Moser, J. E.; Nazeeruddin, M. K.; Sekiguchi, T.; Graetzel, M. *Nat. Mater.* **2003**, *2*, 402.
(3) McConnell, R. D. *Renewable Sustainable Energy Rev.* **2002**, *6*, 273.
(4) Benkstein, K. D.; Kopidakis, N.; van de Lagemaat, J.; Frank, A. J. *J. Phys. Chem. B* **2003**, *107*, 7759.
(5) Hara, K.; Sato, T.; Katoh, R.; Furube, A.; Ohga, Y.; Shinpo, A.; Suga, S.; Sayama, K.; Sugihara, H.; Arakawa, H. *J. Phys. Chem. B* **2003**, *107*, 597.
(6) Nakade, S.; Saito, Y.; Kubo, W.; Kitamura, T.; Wada, Y.; Yanagida, S. *J. Phys. Chem. B* **2003**, *107*, 8607.
(7) Tachibana, Y.; Haque, S. A.; Mercer, I. P.; Moser, J. E.; Klug, D. R.; Durrant, J. R. *J. Phys. Chem. B* **2001**, *105*, 7424.
(8) Moser, J. E.; Noukakis, D.; Bach, U.; Tacchibana, Y.; Klug, D. R.; Durrant, J. R.; Humphry-Baker, R.; Grätzel, M. *J. Phys. Chem. B* **1998**, *102*, 3649.
(9) Boschloo, G.; Lindstrom, H.; Magnusson, E.; Holmberg, A.; Hagfeldt, A. *J. Photochem. Photobiol. A* **2002**, *148*, 11.
(10) Ferrere, S.; Gregg, B. A. *J. Phys. Chem. B* **2001**, *105*, 7602.
(11) Bignozzi, C. A.; Aragazzi, R.; Kleverlaan, C. J. *Chem. Soc. Rev.* **2000**, *29*, 87.
(12) Asbury, J. B.; Anderson, N. A.; Hao, E.; Ai, X.; Lian, T. *J. Phys. Chem. B* **2003**, *107*, 7376.
(13) Oskam, G.; Bergeron, B. V.; Meyer, G. J.; Searson, P. C. *J. Phys. Chem. B* **2001**, *105*, 6867.
(14) Sauvé, G.; Cass, M. E.; Doig, S. J.; Lauermann, I.; Pomykal, K.; Lewis, N. S. *J. Phys. Chem. B* **2000**, *104*, 3488.
(15) De Paoli, M.-A.; Machado, D. A.; Nogueira, A. F.; Longo, C. *Electrochim. Acta* **2001**, *46*, 4243.
(16) Hou, Y.-J.; Xie, P.-H.; Zhang, B.-W.; Cao, Y.; Xiao, X.-R.; Wang, W.-B. *Inorg. Chem.* **1999**, *38*, 6320.
(17) Kumara, G. R. A.; Konno, A.; Shiratsuchi, K.; Tsukahara, J.; Tennakone, K. *Chem. Mater.* **2002**, *14*, 954.
(18) Lemon, B.; Hupp, J. T. *J. Phys. Chem. B.* **1999**, *103*, 3797.
(19) Sakaki, S.; Kuroki, T.; Hamada, T. *J. Chem. Soc., Dalton Trans.* **2002**, 840.
(20) Chen, S. G.; Chappel, S.; Diamant, Y.; Zaban, A. *Chem. Mater.* **2001**, *13*, 4629.

10.1021/ic049906m CCC: $27.50 © 2004 American Chemical Society
Published on Web 06/11/2004

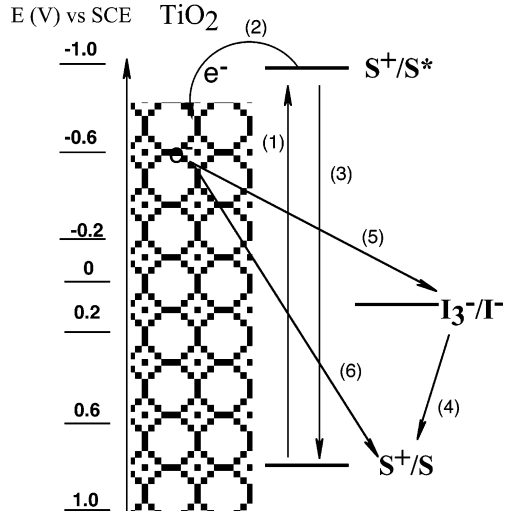

Figure 1. Illustration of the interfacial charge-transfer processes in a nanocrystalline dye-sensitized solar cell. $S/S^+/S^*$ represents the sensitizer in the ground, oxidized, and excited state, respectively. Visible light absorption by the sensitizer (1) leads to an excited state, followed by electron injection (2) onto the conduction band of TiO_2. The oxidized sensitizer (3) gets reduced by the I^-/I_3^- redox couple (4). The electrons injected into the conduction band may react either with the oxidized redox couple (5) or with an oxidized dye molecule (6).

on the nanocrystalline TiO_2 surface. The immobilized dye photoexcitation of the metal-to-ligand charge transfer (MLCT) (eq 1) leads to injection of electrons into the conduction band of the oxide (eq 2). The oxidized dye is subsequently reduced by electron donation from an electrolyte containing the iodide/triiodide redox system (eq 3). The injected electron flows through the semiconductor network to arrive at the back contact and then through the external load to the counter electrode. At the counter electrode, reduction of triiodide regenerates iodide (eq 4) through the donation of electrons from the external circuit, which completes the circuit. However, there are undesirable side reactions: the injected electrons may recombine either with oxidized sensitizer (eq 5) or with the oxidized redox couple at the TiO_2 surface (eq 6), resulting in losses in the cell efficiency. For a net forward current under steady-state illumination, the processes of eq 2 and 3 must be kinetically more favorable than those of eq 5 and 6.

$$\text{S(adsorbed on TiO}_2) + h\nu \rightarrow \text{S*(adsorbed on TiO}_2) \quad (1)$$

$$\text{S*(adsorbed on TiO}_2) \rightarrow \text{S}^+\text{(adsorbed on TiO}_2) + \text{e}^-\text{(injected)} \quad (2)$$

$$\text{S}^+\text{(adsorbed on TiO}_2) + \frac{3}{2}\text{I}^- \rightarrow \text{S(adsorbed on TiO}_2) + \frac{1}{2}\text{I}_3^- \quad (3)$$

$$\text{I}_3^- \text{ (cathode)} + 2\text{e}^- \rightarrow 3\text{I}^- \text{ (cathode)} \quad (4)$$

$$\text{S}^+\text{(adsorbed on TiO}_2) + \text{e}^- \text{ (TiO}_2) \rightarrow \text{S(adsorbed on TiO}_2) \quad (5)$$

$$\text{I}_3^- + 2\text{e}^- \text{ (TiO}_2) \rightarrow 3\text{I}^- \text{ (anode)} \quad (6)$$

The overall conversion efficiency (η) of the dye-sensitized solar cell is determined by the photocurrent density (i_{ph}), the open circuit potential (V_{oc}), the fill factor (*ff*) of the cell, and the intensity of the incident light (I_s), as shown in eq 7.

$$\eta_{\text{global}} = i_{\text{ph}} V_{\text{oc}} \frac{ff}{I_s} \quad (7)$$

In these cells, the dye is one of the key components for high-power conversion efficiencies. The pioneering studies on dye-sensitized solar cells using *cis*-dithiocyanatobis(4,4′-dicarboxylic acid-2,2′-bipyridine)ruthenium(II) (**N3**) are a paradigm in this field.[1,24] A new development for dyes applied to solar cells comes from the preparation of amphiphilic heteroleptic **N3** equivalents.[25] These amphiphilic heteroleptic sensitizers have several advantages compared to the **N3** complex: (a) The ground-state pK_a of the 4,4′-dicarboxy-2,2′-bpy is higher, such that it enhances the binding of the complex onto the TiO_2 surface. (b) The decreased charge on the sensitizer attenuates the electrostatic repulsion and thereby increases the dye loading. (c) The presence of the hydrophobic moiety on the ligand increases the stability of solar cells toward water-induced desorption. (d) The oxidation potential of these complexes is cathodically shifted compared to that of the **N3** sensitizer, which increases the reversibility of the ruthenium III/II couple, leading to enhanced stability.

Our research has focused on the synthesis of novel heteroleptic Ru(II) complexes with amphiphilic structures, using a reliable synthetic protocol and study of their photovoltaic properties in nanocrystalline TiO_2-based solar cells.[2,25] In this paper, we report a one-pot assembly of tailored amphiphilic heteroleptic ruthenium sensitizers, starting from dichloro(*p*-cymene)ruthenium(II) dimer, and their swift deposition onto a TiO_2 surface for dye-sensitized solar cell applications. The complexes were characterized using cyclic and square-wave voltammetry, NMR, UV−visible, and luminescence spectroscopy.

2. Experimental Section

Materials. The solvents (puriss grade, Fluka), hydrated ruthenium trichloride (Johnson Matthey), 4,4′-dimethyl-2,2′-bipyridine (dmbpy), dichloro(*p*-cymene)ruthenium(II) dimer, and potassium/ammonium thiocyanate were obtained (Aldrich) and used as received.

Analytical Measurements. UV/vis and fluorescence spectra were recorded in a 1 cm path length quartz cell on a Cary 5 spectrophotometer and Spex Fluorolog 112 spectrofluorimeter, respectively. Electrochemical data were obtained by cyclic (scan rate 100−1000 mV/s) and square-wave (frequency, 40 Hz; step potential, 1 mV) voltammetry in a conventional three-electrode cell using an AUTOLAB system (PGSTAT 30). A glassy-carbon or a

(21) Xie, P.-H.; Hou, Y. J.; Zhang, B.-W.; Cao, Y.; Wu, F.; Tian, W.-J.; Shen, J. C. *J. Chem. Soc., Dalton Trans.* **1999**, 4217.
(22) Nazeeruddin, M. K.; Zakeeruddin, S. M.; Humphry-Baker, R.; Kaden, T. A.; Grätzel, M. *Inorg. Chem.* **2000**, *39*, 4542.
(23) Rice, C. R.; Ward, M. D.; Nazeeruddin, M. K.; Grätzel, M. *New J. Chem.* **2000**, *24*, 651.
(24) Nazeeruddin, M. K.; Zakeeruddin, S. M.; Humphry-Baker, R.; Jirousek, M.; Liska, P.; Vlachopoulos, N.; Shklover, V.; Fischer, C. H.; Grätzel, M. *Inorg. Chem.* **1999**, *38*, 6298.
(25) Zakeeruddin, S. M.; Nazeeruddin, M. K.; Humphry-Baker, R.; Péchy, P.; Quagliotto, P.; Barolo, C.; Viscardi, G.; Graetzel, M. *Langmuir* **2002**, *18*, 952.

gold working electrode, glassy-carbon auxiliary electrode, and silver rod as a quasi-reference electrode were used in a single-compartment configuration. Cyclic voltammograms of complexes **5**−**8** were obtained from 1 mM solutions of each complex in DMF, containing 0.1 M tetrabutylammonium perchlorate. The solution was deaerated by bubbling argon gas through it. The electrochemical data of complexes adsorbed on TiO_2 were obtained under conditions similar to those used for the solution cyclic voltammograms. After each measurement, the ferrocene cyclic voltammogram was recorded, and the reported potentials were referenced against the ferrocenium/ferrocene couple (Fc^+/Fc).

^1H and ^{13}C NMR spectra were measured on a Bruker 200 MHz spectrometer. The reported chemical shifts were in ppm against tetramethylsilane (TMS). The Fourier transform infrared (FTIR) spectra for all the samples were measured using a Digilab 7000 FTIR spectrometer. The attenuated total reflection-Fourier transform infrared (ATR-FTIR) data reported here were taken with the "Golden Gate" diamond anvil ATR accessory (Graseby-Specac), using typically 64 scans at a resolution of 2 cm^{-1}. The samples were all measured under the same mechanical force pushing the samples in contact with the diamond window. No ATR correction has been applied to the data. It also has to be appreciated that this ATR technique probes, at most, 1 μm of sample depth, and that this depends on the sample refractive index, porosity, etc. The IR optical bench was flushed with dry air. The dye-coated TiO_2 films were rinsed in acetonitrile and dried at 150 °C before the spectra were taken. The FTIR spectra of anchored dyes were obtained by subtracting the IR spectrum of the blank TiO_2 films from the IR spectrum of the dye-coated TiO_2 films of the same thickness.

TiO_2 Electrode Preparation. TiO_2 anatase nanoparticles of 16 nm were prepared by hydrolysis of titanium(IV) isopropoxide, as described before.[26] The nanocrystalline TiO_2 thin films of 12 μm thickness were deposited onto transparent conducting glass (TEC-15, which has been coated with a fluorine-doped stannic oxide layer, with a sheet resistance of 12−15 Ω/cm^2) by screen printing. These films were dried at 150 °C for 20 min and then a 4 μm thick layer of 400 nm TiO_2 particles (400 nm particles were obtained from CCI, Japan) was deposited again using a screen printing method. The double-layered films were sintered at 500 °C for 20 min.

The heated electrodes were impregnated with a 0.05 M titanium tetrachloride solution in a water-saturated desiccator for 30 min at 70 °C and washed with distilled water. The 0.05 M titanium tetrachloride solution was prepared in the following manner: First, a 2 M titanium tetrachloride solution was prepared by adding directly titanium tetrachloride liquid into a bottle containing ice, which was cooled to −20 °C, and then the solution was further diluted to 0.05 M. Finally, the electrodes were heated at 520 °C for 20 min and allowed to cool to 50 °C before being dipped into the dye solution.

Dye solutions were prepared in the concentration range of (2−3) × 10^{-4} M in ethanol, and the electrodes were dipped into the dye solution for 18−22 h. Alternatively, the heated TiO_2 electrodes were dipped for 20−30 min into a concentrated dye solution of 9 × 10^{-3} M in dimethylformamide (DMF), or a measured volume of 9 × 10^{-3} M solution in DMF was pipetted (10 μL for 0.5 cm^2 TiO_2 area) onto the surface of the TiO_2 electrode and the dye solution left for 30 min.[27] The dye-coated electrodes were rinsed quickly with acetonitrile and used as such for photovoltaic measurements.

Dye-Sensitized Solar Cell Fabrication. The dye-deposited film is used as a working electrode. A sandwich cell was prepared with a second conducting glass coated with chemically deposited platinum from 0.05 M hexachloroplatinic acid. The platinum-coated counter electrode and the dye-coated TiO_2 films were then put together with a thin transparent film of Surlyn polymer frame (DuPont). The sandwiched electrodes were tightly held, and then heat (130 °C) was applied around the Surlyn frame to seal the two electrodes. A thin layer of electrolyte, consisting of 0.6 M butylmethylimidazolium iodide (BMII), 0.05 M I_2, 0.1 M LiI, and 0.5 M *tert*-butylpyridine in 1:1 acetonitrile/valeronitrile, was introduced into the inter-electrode space from the counter electrode side through predrilled holes. The drilled holes were sealed with a microscope cover slide and Surlyn to avoid leakage of the electrolyte solution.

Photoelectrochemical Measurements. Photoelectrochemical data were measured using a 450 W xenon light source that was focused to give 1000 W/m^2, the equivalent of one sun at Air Mass (AM) 1.5, at the surface of the test cell. The spectral output of the lamp was matched in the region of 350−750 nm with the aid of a Schott KG-5 sunlight filter, so as to reduce the mismatch between the simulated and the true solar spectrum to less than 2%. The differing intensities were regulated with neutral wire mesh attenuators. The applied potential and measured cell current were measured using a Keithley model 2400 digital source meter. The current−voltage characteristics of the cell under these conditions were determined by biasing the cell externally and measuring the generated photocurrent. This process was fully automated using Wavemetrics software. A similar data acquisition system was used to control the incident photon-to-current conversion efficiency (IPCE) measurement. Under full computer control, light from a 300 W Xe lamp was focused through a high-throughput monochromator onto the photovoltaic cell under test. The photoelectrochemical properties were investigated by measuring the current and voltage ($I-V$) characteristics.

3. Synthesis and Characterization

3.1. Ligands. 4,4′-Bis(1-adamantyl-aminocarbonyl)-2,2′-bipyridine (L^1). Compound L^1 was synthesized with slight modification of the published method.[28] Anal. Found: C, 68.15; H, 7.74; N, 9.87. Calcd for $C_{32}H_{38}N_4O_2 \cdot 3H_2O$: C, 68.07; H, 7.85; N, 9.92.

4,4′-Bis{5-{*N*-[2-(3β-cholest-5-en-3-ylcarbamate-*N*-yl)ethyl]-aminocarbonyl}}-2,2′-bipyridine (L^2) and 4,4′-Bis{5-{*N*-[2-(3β-cholest-5-en-3-ylcarbamate-*N*-yl)propyl]aminocarbonyl}}-2,2′-bipyridine (L^3). 3β-Cholest-5-en-3-yl-*N*-(2-aminoethyl)carbamate (**2a**) and 3β-cholest-5-en-3-yl-*N*-(3-aminopropyl)carbamate (**3a**) were synthesized according to the published method, with the following modifications.[29] Cholesteryl chloroformate (1 g, 2.2 mmol) was added portion-wise to 20 mL of freshly distilled diamine under argon at room temperature. The resulting gel was stirred for 30 min, before being diluted with 5 mL of dry toluene via syringe. Stirring was continued overnight at room temperature. CH_2Cl_2 (200 mL) and dilute $KHCO_3$ solution (100 mL) were then successively added. The organic phase was separated, washed with dilute $KHCO_3$ solution (100 mL), washed with water (2 × 100 mL), dried over $MgSO_4$, and evaporated to dryness to afford **2a** (968 mg, 92%) or

(26) Nazeeruddin, M. K.; Péchy, P.; Renouard, T.; Zakeeruddin, S. M.; Humphry-Baker, R.; Comte, P.; Liska, P.; Le, C.; Costa, E.; Shklover, V.; Spiccia, L.; Deacon, G. B.; Bignozzi, C. A.; Graetzel, M. *J. Am. Chem. Soc.* **2001**, *123*, 1613.
(27) Nazeeruddin, M. K.; Splivallo, R.; Liska, P.; Comte, P.; Grätzel, M. *Chem. Chommun.* **2003**, 1456.
(28) Hamada, T.; Tanaka, S. I.; Koga, H.; Sakai, Y.; Sakaki, S. *J. Chem. Soc., Dalton Trans.* **2003**, *4*, 692.
(29) Ishi-i, T.; Iguchi, R.; Snip, R.; Ikeda, M.; Shinkai, S. *Langmuir* **2001**, *17*, 5825.

3a (867 mg, 80%) as a white solid. Spectroscopic data are in agreement with those already published. The general procedure for the preparation of 4,4′-bis{5-{*N*-[2-(3β-cholest-5-en-3-ylcarbamate-*N*-yl)ethyl]aminocarbonyl}}-2,2′-bipyridine (**L²**) and 4,4′-bis{5-{*N*-[2-(3β-cholest-5-en-3-ylcarbamate-*N*-yl)propyl]aminocarbonyl}}-2,2′-bipyridine (**L³**) is as follows. 4,4′-bis(chlorocarbonyl)-2,2′-bipyridine (200 mg, 0.7 mmol) was added in one portion to a stirred solution of **2a** (838 mg, 1.8 mmol) or **3a** (867 mg, 1.8 mmol) in 25 mL of dry toluene at 50 °C under argon. After 10 min, 0.3 mL of Et_3N was added to the mixture via syringe. The resulting gel-like mixture was stirred at 50 °C overnight. CH_2Cl_2 (200 mL) and dilute $KHCO_3$ solution (100 mL) were then successively added. The organic phase was separated and washed with dilute $KHCO_3$ solution (2 × 100 mL), washed with water (2 × 100 mL), dried over $MgSO_4$, and evaporated to dryness. The resulting solid was then dissolved in 30 mL of boiling $CHCl_3$ and precipitated by addition of 100 mL of acetone. The precipitate was collected by filtration and washed several times with acetone to afford **L²** (665 mg, 81%) as a slightly pink solid or **L³** (671 mg, 80%) as a white solid. Due to the low solubility of these two compounds in all organic solvents, ^{13}C analyses were not performed. **L²**: ^1H NMR ($CDCl_3$, 298 K, 200 MHz, δ in ppm) 0.69 (s, 6H), 0.86 (s, 6H), 0.90 (s, 6H), 0.91−2.20 (m, 64H), 2.30−2.38 (m, 4H), 3.45−3.53 (m, 4H), 3.60−3.67 (m, 4H), 4.50−4.60 (m, 2H), 5.10−5.11 (m, 2H), 5.31 (d, J = 4.7 Hz, 2H), 7.48−7.52 (m, 2H), 7.79 (d, J = 5 Hz, 2H), 8.76 (s, 2H), 8.82 (d, J = 5 Hz, 2H). Anal. found: C, 73.22; H, 9.58; N, 7.1. Calcd for $C_{72}H_{108}N_6O_6 \cdot 1.5H_2O$: C, 73.24; H, 9.98; N, 7.4. **L³**: ^1H NMR ($CDCl_3$, 298 K, 200 MHz, δ in ppm) 0.69 (s, 6H), 0.86 (s, 6H), 0.90 (s, 6H), 0.91−2.20 (m, 68H), 2.20−2.42 (m, 4H), 3.30−3.35 (m, 4H), 3.50−3.60 (m, 4H), 4.52−4.57 (m, 2H), 5.00−5.07 (m, 2H), 5.37 (d, J = 4.7 Hz, 2H), 7.46−7.52 (m, 2H), 7.81 (dd, J = 5, 1.8 Hz, 2H), 8.79 (s, 2H), 8.83 (d, J = 5 Hz, 2H). Anal. Found: C, 70.81; H, 9.86; N, 6.67. Calcd for $C_{74}H_{112}N_6O_6 \cdot 4H_2O$: C, 70.89; H, 9.64; N, 6.7.

Synthesis of 4,4′-Bis(dodecan-12-ol)-2,2′-bipyridine (L⁴). LDA (2M, 3 mL, 6 mmol) was added dropwise under argon to a solution of 4,4′-dimethyl-2,2′-bipyridine (500 mg, 2.7 mmol) in 45 mL of dry THF at −78 °C. The resulting brown-red solution was stirred at this temperature for 1 h before the addition of 1-tetrahydropyranyl-11-bromoundecane[30] (2.1 g, 6.3 mmol), dissolved in 5 mL of dry THF. The resulting mixture was stirred at −78 °C for 15 min, allowed to warm to room temperature (≈1 h), and stirred 1 h at this temperature before the THF was evaporated. The resulting residue was flash chromatographed (SiO_2, CH_2Cl_2/MeOH/Et_3N, 98:1:1). The obtained yellow-brown oil was triturated in 5 mL of acetone. The formed precipitate was filtered off and washed with small portions of cold acetone to afford 800 mg of pure 4,4′-bis(dodecan-12-ol)-2,2′-bipyridine as a white solid. Evaporation of the filtrate and precipitation with acetone afforded a second crop of 400 mg (64%). ^1H NMR ($CDCl_3$, 298 K, 200 MHz, δ in ppm) 1.26−1.71 (m, 52H), 2.70 (t, J = 7 Hz, 4H), 3.20−3.55 (m, 4H), 3.78−3.95 (m, 4H), 4.58 (m, 2H), 7.14 (d, J = 5 Hz, 2H), 8.23 (s, 2H), 8.56 (d, J = 5 Hz, 2H). ^{13}C NMR ($CDCl_3$, 298 K, 50 MHz, δ in ppm) 8.6, 19.7, 25.5, 26.2, 29.3, 29.4, 29.5, 29.6, 29.7, 30.4, 30.8, 35.5, 46.0, 62.3, 67.7, 98.8, 121.3, 123.8, 148.9, 152.9, 156.1.

4,4′-Bis(12-tetrahydropyranyl-dodecane)-2,2′-bipyridine (1.2 g, 1.73 mmol) was stirred at room temperature in a mixture of MeOH/H_2O/concentrated HCl (40:9:1, v/v/v) for 6 h. After the evaporation of the methanol, water (100 mL) and CH_2Cl_2 (200 mL) were added. The organic layer was separated, washed with $KHCO_3$ (5%), dried over $MgSO_4$, and evaporated to afford 0.85 g (93%) of 4,4′-bis-(dodecan-12-ol)-2,2′-bipyridine as a white solid. ^1H NMR ($CDCl_3$, 298 K, 200 MHz, δ in ppm) 1.26−1.78 (m, 40H), 2.70 (t, J = 7 Hz, 4H), 3.64 (t, J = 7 Hz, 4H), 7.14 (d, J = 5 Hz, 2H), 8.23 (s, 2H), 8.56 (d, J = 5 Hz, 2H). ^{13}C NMR ($CDCl_3$, 298 K, 50 MHz, δ in ppm) 8.6, 25.7, 29.2, 29.3, 29.4, 29.5, 29.6, 30.4, 32.8, 35.5, 45.8, 63.0, 121.3, 123.9, 148.9, 153.0, 156.0. Anal. Found: C, 77.55; H, 10.39; N, 5.5. Calcd for $C_{34}H_{56}N_2O_2$: C, 77.81; H, 10.76; N, 5.34.

3.2. Complexes. Synthesis of [Ru(II)LL¹(NCS)₂] (5) (Where L = 4,4′-Bis(carboxylic acid)-2,2′-bipyridine and L¹= 4,4′-Bis-(1-adamantyl-aminocarbonyl)-2,2′-bipyridine). A mixture of ligand **L¹** (200 mg, 0.4 mmol) and dichloro(*p*-cymene)ruthenium-(II) dimer (120 mg, 0.2 mmol) in argon-degassed DMF (25 mL) was heated at 100 °C for 4 h. 4,4′-Bis(carboxylic acid)-2,2′-bipyridine (98 mg, 0.4 mmol) was then added, and the reaction was refluxed at 160 °C for 4 h. After this was added NH_4NCS (304 mg, 4 mmol), and the solution was refluxed for a further 4 h at 140 °C. After evaporation of the DMF, the resulting purple residue was suspended in water (150 mL) and sonicated for 5 min. The solution pH was adjusted to 4 with HNO_3 (0.2 M), and the mixture was left to stand in a refrigerator overnight at −4 °C. The resulting purple solid was then filtered and successively washed with water and diethyl ether. The crude complex was purified on a Sephadex LH-20 column of 2 × 30 cm, using methanol as an eluent. Anal. Calc for $C_{46}H_{46}N_8O_6RuS_2$: C, 56.83; H, 4.77; N, 11.53. Found: C, 56.74; H, 5.03; N, 11.54. ^1H NMR (δ_H(ppm) in CD_3OD, J(Hz)) 9.59 (d, $H^{6,5}$, J = 5.8), 9.49 (d, $H^{6',5'}$), 9.05 (s, H^{3}), 8.97 (s, $H^{3'}$), 8.89 (s, $H^{3''}$), 8.8 (H, s, $H^{3'''}$), 8.31 (dd, $H^{5,6,3}$, J = 5.8, 2), 8.13 (dd, $H^{5,6,3}$, J = 5.8, 2), 7.76 (d, $H^{6'',5''}$, J = 5.9), 7.73 (d, $H^{6''',5'''}$, J = 5.9), 7.65 (dd, $H^{5'',6''}$, J = 5.9, 2), 7.46. Aliphatic protons: 3.31, 2.16, 1.66, 1.61, 1.52, 1.06.

Synthesis of [Ru(II)LL²(NCS)₂] (6) (Where L = 4,4′-Bis-(carboxylic acid)-2,2′-bipyridine and L² = 4,4′-Bis{5-{*N*-[2-(3β-cholest-5-en-3-ylcarbamate-*N*-yl)ethyl]aminocarbonyl}}-2,2′-bipyridine). Using the same conditions as for complex **5**, except using anhydrous DMF and starting from ligand **L²**, the title compound was obtained. The resulting purple solid was then filtered and successively washed with water and diethyl ether. The crude complex was purified on a Sephadex LH-20 column of 2 × 30 cm, using DMF as an eluent. Anal. Calcd for $C_{86}H_{116}N_{10}O_{10}RuS_2$: C, 64.14; H, 7.3; N, 8.6. Found: C, 64.42; H, 7.53; N, 8.81. ^1H NMR (δ_H(ppm) in CD_3OD, J(Hz)) 9.66 (d, $H^{6,5}$), 9.63 (d, $H^{6',5'}$), 9.05 (s, H^{3}), 9.05 (s, $H^{3'}$), 8.89 (s, $H^{3''}$), 8.8 (H, s, $H^{3'''}$), 8.28 (d, $H^{5,6}$), 8.25 (d, $H^{5',6'}$), 7.86 (d, $H^{6'',5''}$), 7.67 (d, $H^{6''',5'''}$), 7.64 (d, $H^{5'',6''}$, J = 5.9), 7.56 (d, $H^{5''',6'''}$). Aliphatic protons: several multiplets due to [(3β-cholest-5-en-3-ylcarbamate-*N*-yl)ethyl]amine between 3.81 and 1 ppm.

Synthesis of [Ru(II)LL³(NCS)₂] (7) (Where L = 4,4′-Bis-(carboxylic acid)-2,2′-bipyridine and L³ = 4,4′-bis{5-{*N*-[2-(3β-cholest-5-en-3-ylcarbamate-*N*-yl)propyl]aminocarbonyl}}-2,2′-bipyridine). Using the same conditions as for complex **6**, starting from the ligand 4,4′-bis{5-{*N*-[2-(3β-cholest-5-en-3-ylcarbamate-*N*-yl)propyl]aminocarbonyl}}-2,2′-bipyridine, the title compound was obtained. The crude complex was purified on a Sephadex LH-20 column of 2 × 30 cm, using DMF as an eluent. Anal. Calc for $C_{88}H_{120}N_{10}O_{10}RuS_2$: C, 64.32; H, 7.36; N, 8.52. Found: C, 64.42; H, 7.41; N, 8.67. ^1H NMR (δ_H(ppm) in CD_3OD, J(Hz)) 9.56 (d, $H^{6,5}$), 9.5 (d, $H^{6',5'}$), 9.05 (s, H^{3}), 8.89 (s, $H^{3'}$), 8.86 (s, $H^{3''}$), 8.3 (H, s, $H^{3'''}$), 8.16 (d, $H^{5,6}$), 8.05 (d, $H^{5',6'}$), 7.86 (d, $H^{6'',5''}$), 7.66 (d, $H^{6''',5'''}$), 7.62 (d, $H^{5'',6''}$, J = 5.9), 7.52 (d, $H^{5''',6'''}$). Aliphatic protons: several multiplets due to [(3β-cholest-5-en-3-ylcarbamate-*N*-yl)propyl] amine between 3.81 and 1 ppm.

(30) Srisiri, W.; Lee, Y. S.; Sisson, T. M.; Bondurant, B.; O'Brien, D. F. *Tetrahedron* **1997**, *53*, 15397.

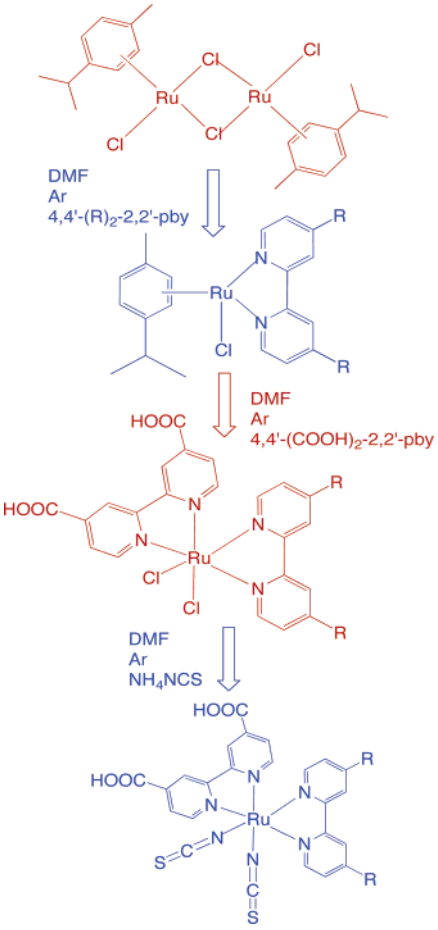

Figure 2. Synthetic strategy adopted for the preparation of cis-amphiphilic heteroleptic complexes.

Synthesis of [Ru(II)LL^4(NCS)$_2$] (8) (Where L = 4,4′-Bis-(carboxylic acid)-2,2′-bipyridine and L^4 = 4,4′-bis(dodecan-12-ol)-2,2′-bipyridine). Using the same conditions as for complex **5**, starting from the ligand 4,4′-bis(dodecan-12-ol)-2,2′-bipyridine, the title compound was obtained. The resulting purple solid was then filtered, washed with water, and washed with Et_2O. Purification on a Sephadex LH-20 column using methanol as an eluent afforded the desired complex as a dark purple solid. Anal. Calcd for $C_{48}H_{64}N_6O_6RuS_2$: C, 58.45; H, 6.54; N, 8.52. Found: C, 56.66; H, 6.39; N, 8.58. ^{1}H NMR (δ_H(ppm) in CD_3OD, J(Hz)) 9.68 (d, H^{6,5}, J = 5.8), 9.27 (d, H$^{6',5'}$), 9.05 (s, H^{3}), 8.89 (s, H$^{3'}$), 8.52 (s, H$^{3''}$), 8.38 (H, s, H$^{3'''}$), 8.25 (dd, H^{5,6,3}, J = 5.8,1), 7.9 (d, H$^{6'',5''}$, J = 5.8), 7.70 (d, H$^{5',6'}$, J = 5.9), 7.66 (d, H$^{5'',6''}$, J = 5.9), 7.39 (d, H$^{6''',5'''}$, J = 5.9, 2), 7.04, (d, H$^{5''',6''',3'''}$, J = 5.9, 1). Aliphatic protons: 3.57 (t), 3.52 (t), 2.99 (t), 2.73(t), 1.9 (m), 1.65 (m), 1.55 (m), 1.35 (m).

4. Results and Discussion

Synthetic Studies. Figure 2 shows the details of the synthetic strategy adopted for the preparation of heteroleptic complexes of the type [Ru(L)(L^x)(NCS)$_2$], where L = 4,4′-bis(carboxylic acid)-2,2′-bipyridine and L^x = (**L^1**), (**L^2**), (**L^3**), or (**L^4**). During the reaction, aliquots of the intermediate products were withdrawn and characterized by NMR and UV/vis spectra. Reaction of dichloro(*p*-cymene)ruthenium-(II) dimer in *N*,*N*′-dimethylformamide (DMF) solution at 100 °C with L^x resulted a mononuclear complex. In this step, coordination of the substituted bipyridine ligand to the ruthenium center takes place with cleavage of the doubly chloride-bridged structure of the dimeric complex.[31]

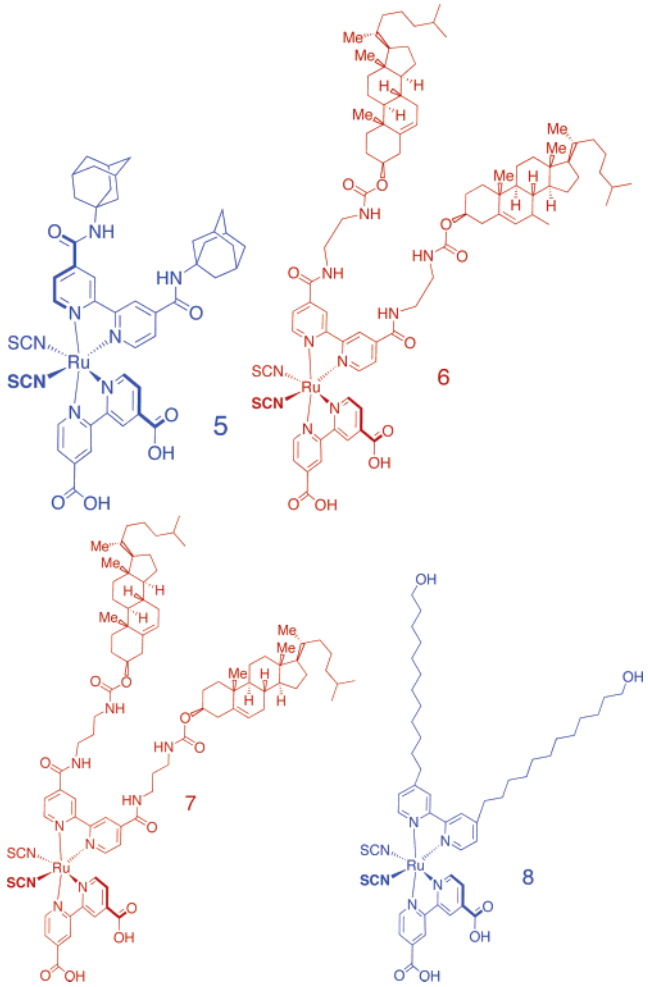

Figure 3. Structures of complexes **5**−**8**.

The heteroleptic dichloro complexes were prepared by reacting the mononuclear [Ru(L^x)Cl(cymene)]Cl complex with L under reduced light at 160 °C. The UV/vis spectral properties of [Ru(L)(L^x)(Cl)$_2$] are identical to those of the similar complexes prepared by using the $RuCl_2(DMSO)_4$ method.[25] It is interesting to note that the displacement of the cymene ligand from the coordination sphere of ruthenium metal by substituted bipyridine ligand takes place efficiently in organic solvents (ethanol and DMF), even in the dark at 80 °C. The [Ru(L)(L^x)(Cl)$_2$] complex was reacted with a 30-fold excess of ammonium thiocyanate ligand to obtain the [Ru(L)(L^x)(NCS)$_2$] complex.

The NMR spectra of the isolated complexes show the presence of ≈95% N-bonded and ≈5% S-bonded isomers, which were separated on a Sephadex LH-20 column of 2 × 30 cm, using methanol or DMF as an eluent. The complexes **5**−**8** are insoluble in water and soluble in organic solvents, such as alcohols, nitriles, and DMF. However, complexes **6** and **7** are highly soluble in chlorinated solvents, such as $CHCl_3$ and CH_2Cl_2. Figure 3 shows the chemical structures of the complexes **5**−**8**.

(31) Wendicke, S. B.; Burri, E.; Scopelliti, R.; Severin, K. *Organometallics* **2003**, *22*, 1894.

Table 1. Absorption, Photophysical, and Electrochemical Properties of the Ruthenium Complexes

complex	abs max (nm)[a] (ϵ/10^4 M^{-1} cm^{-1}) $\pi-\pi^*$	abs max (nm)[a] (ϵ/10^4 M^{-1} cm^{-1}) $d\pi-\pi^*$	emiss.[b] λ_{max} (nm)	$E_{1/2}$ Ox[c] $Ru^{III/II}$ (ΔE)/V	$E_{1/2}$ reduction[d] (ΔE)/V L	$E_{1/2}$ reduction[d] (ΔE)/V L′
5	313 (3.88)	392 (1.17) 537 (1.19)	818	0.38	−1.78	−2.32
6	314 (3.36)	390 (1.11) 531 (1.12)	750	0.38	−1.76	−2.31
7	312 (3.39)	393 (1.12) 533 (1.21)	771	0.39	−1.75	−2.31
8	297 (4.54) 309 (2.74)	370 (1.25) 522 (1.26)	800	0.29	−2.10	−2.43
N3	314 (4.82)	398 (1.4) 539 (1.42)	830	0.4	−1.90	

[a] The data correspond to the protonated complexes measured in DMF. [b] Emission data are obtained at room temperature in DMF by exciting at the lowest-energy MLCT band at 530 nm without degassing. The error of the recorded values is ±2 nm. [c] The electrochemical data are measured in DMF solvent with 0.1 M tetrabutylammonium perchlorate, using a gold (or glassy-carbon) electrode and referenced against the ferrocene/ferrocinium couple. Under identical conditions, the ferrocene/ferrocinium couple was observed at 0.46 V vs SCE, with a 70 mV separation between the anodic and cathodic peaks. [d] The first reduction is due to dcbpy, and the second reduction is due to substituted bpy.

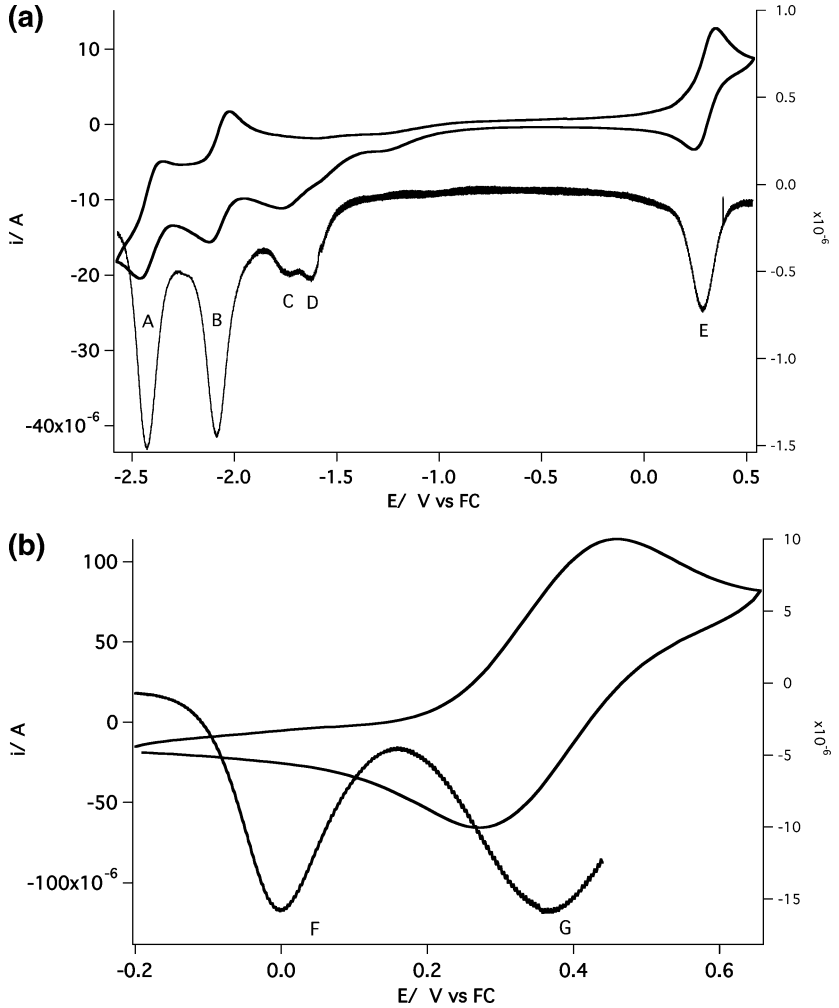

Figure 4. (a) Cyclic voltammogram (scan speed of 100 mV/s) and the square-wave voltammogram (frequency of 40 Hz and step potential of 1 mV) of complex **8**, measured in a DMF solution containing 0.1 M TBA(ClO_4) using a gold electrode. (b) Cyclic voltammogram (scan speed of 100 mV/s) and the square-wave voltammogram (frequency of 40 Hz and step potential of 1 mV) of complex **8** adsorbed on TiO_2 electrode in a DMF solution containing 0.1 M TBA(ClO_4).

Electrochemical Data. The oxidation and reduction potential data of complexes **5**−**8**, obtained using a gold or glassy-carbon electrode in DMF solvent with 0.1 M tetrabutylammonium perchlorate, are collected in Table 1. In general, the complexes each display one metal-based oxidation and two ligand-based reduction couples within the solvent window. The cyclic voltammograms of complexes **5**−**8** are typical for so-called quasi-reversible behavior associated with a peak separation of 0.09 V, rather than the 0.059 V expected for the reversible case. Figure 4 shows the cyclic voltammogram of complex **8**, measured using a gold electrode with a scan rate of 100 mV/s. Upon scanning to positive potentials, a reversible couple at $E_{1/2} = 0.29$ V vs FC (ferrocene), with a separation of 0.09 V between the anodic and the cathodic peak, was observed due to the $Ru^{II/III}$ couple (Figure 4a, process E). The ruthenium oxidation potential in complex **8** is shifted cathodically by 0.11 V, compared to that of the *cis*-dithiocyanatobis(4,4′-dicarboxylic

acid-2,2′-bipyridine)ruthenium(II) couple (**N3**). The difference (0.11 V) in the oxidation potential of complex **8** compared to that of **N3** is due to the donor influence of 4,4′-bis(dodecan-12-ol)-2,2′-bipyridine to ruthenium metal.

When scanning toward negative potentials with complex **8**, two irreversible (labeled as C and D in Figure 4a) and two reversible waves (labeled as A and B in Figure 4a) were observed. The two irreversible waves, C and D, are assigned to the reduction of OH and carboxylic acid protons to hydrogen of 4,4′-bis(dodecan-12-ol)-2,2′-bipyridine and 4,4′-dicarboxylic acid-2,2′-bipyridine. Wolfbauer et al. have observed a similar reduction-of-proton behavior of the dcbpyH_2 ligand in the **N3** complex at a platinum electrode.[32] However, on a gold electrode, the processes C and D are significantly smaller and shifted more cathodically. The two reversible waves at $E_{1/2} = -2.1$ and -2.43 V vs FC are assigned to the reduction of 4,4′-dicarboxylic acid-2,2′-bipyridine and 4,4′-bis(dodecan-12-ol)-2,2′-bipyridine ligand, respectively (Figure 4a, processes B and A). The separation between the anodic and the cathodic peaks of couples B and A is 0.08 V. The metal-based oxidation and the ligand-based reduction couples in complexes **5**, **6**, and **7** are shifted anodically, compared to complex **8**, due to presence of electron acceptor ligands $\mathbf{L^1}$, $\mathbf{L^2}$, and $\mathbf{L^3}$ (Table 1).

Figure 4b shows the electrochemical properties of complex **8** adsorbed on a thin (2 μm) film of conducting TiO_2 electrode. The voltammogram shows that the metal-centered oxidation potential has shifted anodically (0.07 V) compared to the solution potential due to the interaction of carboxylate groups (anchoring) with the TiO_2 surface. The separation between the anodic peak and the cathodic peak of adsorbed complex **8** is significantly larger (0.18 V) than that of complex **8** in solution, which is most likely due to the resistances at the ITO/TiO_2 interface and the TiO_2 crystal boundary.

The square-wave voltammograms of complex **8** measured in solution and adsorbed onto a TiO_2 electrode are shown in Figure 4a and b, respectively. The observed peak of the square-wave voltammogram at $E_{1/2} = 0$ V in Figure 4b, labeled as F, is due to the ferrocenium/ferrocene couple, which is used as an internal standard. The wave at 0.36 V, labeled as G in Figure 4b, is due to the adsorbed complex **8** couple. Our data of complex **8** adsorbed on a TiO_2 surface are consistent with the literature.[33]

NMR Spectral Data. The NMR spectra of transition metal complexes of the type [Ru(L)(L^x)($NCS)_2$] are extremely useful to identify purity and geometric isomers (cis and trans). Because of the symmetry, the trans isomer of the [Ru(L)(L^x)($NCS)_2$] complex shows six peaks in the aromatic region, corresponding to two different pyridine ring protons. In cis-heteroleptic complexes, the symmetry is lowered when compared to that of cis-homoleptic complexes. In the cis geometry, two different bidentate ligands coordinate to a metal center, in which two pyridyl rings are trans to the

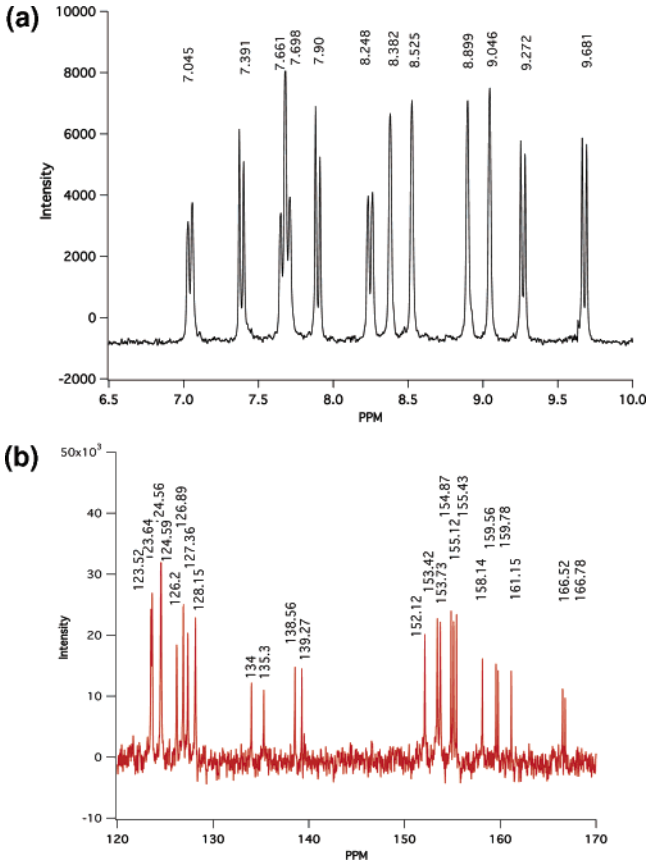

Figure 5. (a) Part of the ^{1}H NMR spectrum of complex **8** in CD_3OD. For clarity, the peaks in the aliphatic region are not included. (b) Part of the ^{13}C NMR spectrum of complex **8** measured in CD_3OD solvent.

thiocyanate ligands and two are trans to each other, resulting in four magnetically nonequivalent pyridyl-ring protons. Hence, the NMR spectrum of heteroleptic complexes is much more complicated (Figure 5a). The ^{1}H NMR spectra of complexes **5**−**8** show 12 sharp and well-resolved signals in the aromatic region, corresponding to the four pyridyl-ring protons. For complex **8**, the aliphatic region shows methylene resonance peaks (not shown in Figure 5a) corresponding to two different groups of 4,4′-bis(dodecan-12-ol)-2,2′-bipyridine)4,4′-dimethyl-2,2′-bipyridine. The aliphatic regions of the NMR spectra of complexes **6** and **7** show several multiplets due to the presence of cholesterol-ring protons.

Figure 5b shows a portion of (δ 170−120 ppm) the ^{13}C NMR spectra of complex **8**, which exhibits 24 resonance signals. In complex **8**, two halves of each ligand are in different magnetic environments and show 22 resonance peaks in the aromatic region due to four pyridyl-ring carbons. The two resonance peaks at 166.78 and 166.52 ppm are due to the two carboxylic acid groups, which are trans to NCS and trans to the pyridyl unit. A set of four peaks between 161 and 158 ppm is assigned to the quaternary carbons of C2, C2′, C2″, and C2‴. The second set of four resonance signals between 155.43 and 153.73 ppm is assigned to C6, C6′, C6″, and C6‴. The two peaks at 153.42 and 152.12 ppm are assigned to C4 and C4′ of carboxy-2,2′-bpy. The peaks at 139.27 and 138.56 ppm were assigned to C4 and C4′ of alkyl-2,2′-bpy. The eight resonance peaks around 125

(32) Wolfbauer, G.; Bond, A. M.; Deacon, G. B.; MacFarlane, D. R.; Spiccia, L. *J. Am. Chem. Soc.* **2000**, *122*, 130.
(33) Heimer, T. A.; D'Arcangelis, S. T.; Farzad, F.; Stipkala, J. M.; Meyer, G. J. *Inorg. Chem.* **1996**, *35*, 5319.

Table 2. Selected ATR-FTIR Data (cm^{-1}) of Complexes **5**−**8** Measured as Powders

group	complex **5**	complex **6**	complex **7**	complex **8**
−OH stretch	3400	3332	3443	3428
−NH stretch	3075	2975	2978	
−CH stretch	2975	2975	2978	2980
$-CH_3$ stretch	2905	2931	2931	2919
$-CH_2$ stretch	2850	2866	2867	2849
−SC═N stretch	2097	2101	2101	2100
>C═O stretch	1720	1687	1700	1690
amide stretch >C═O	1652	1652	1651	
ring modes	1609, 1530, 1467, 1403	1653, 1533, 1465, 1405	1653, 1533, 1466,1409	1611, 1546, 1462, 1405
>C−O stretch	1231	1231	1235	1229
−S═CN stretch	761	768	765	770

ppm are due to C3 and C5 carbons, and no attempts were made to identify individual carbons.

The two peaks at 135.3 and 134 ppm are due to two NCS ligands, which are trans to the carboxylic acid pyridine and alkyl-substituted pyridine, respectively. ^{13}C NMR spectra of complexes containing NCS ligands are useful to identify the mode of coordination of thiocyanate ligand. The N-coordinated thiocyanate carbon resonance peak has been reported in a number of complexes at 130−135 ppm.[34] In complexes **5**−**8**, the two peaks at 136−133 ppm are due to the N-coordinated thiocyanate ligand, which is trans to two different pyridyl ligands. The peaks between 10 and 50 ppm (not shown in the figure) are due to the aliphatic resonance carbon signals.

ATR-FTIR Spectral Data. ATR-FTIR spectra of complexes **5**−**8**, as solids, were measured and the stretching frequencies are collected in Table 2. The bands due to the stretching frequency of υ(CN) group can be used for characterization of the mode of coordination (N-bonded or S-bonded) to the metal ions. The CN of an N-bonded thiocyanate is usually found to be around 2100 cm^{-1}. The bands corresponding to the stretching frequency υ(C−S) of N-coordinated NCS was found between 760 and 770 cm^{-1} for complexes **5**−**8**. The spectra show a strong, broad stretch in the 1700 cm^{-1} region due to the carboxylic acid groups. The intense peak in the region of 1230 cm^{-1} is due to the υ(C−O) stretch.[35]

ATR-FTIR spectroscopy has been shown to be a powerful tool to extract structural information about the metal complexes adsorbed onto the TiO_2 surface.[36] ATR-FTIR spectra of the adsorbed complex **8** on TiO_2 film show the presence of carboxylate asymmetric 1648 cm^{-1} $\upsilon(-COO^-_{as})$ and symmetric 1385 cm^{-1} $\upsilon(-COO^-_s)$ bands, together with a strong υ(NC) of the thiocyanate group at 2100 cm^{-1}. The presence of carboxylate bands in the IR spectra of adsorbed complexes on TiO_2 testifies that the two carboxylic acid groups are dissociated and involved in the adsorption on the TiO_2 surface. Representative ATR-FTIR spectra of complex **8**, measured as a solid and in the TiO_2-adsorbed form, are shown in Figure 6.

For sensitizers containing carboxylic acid groups, several binding modes (as a unidentate and/or as a chelating and/or as a bridging bidentate) are possible on the TiO_2 surface, as shown in Scheme 1. The unidentate coordination of the carboxylate group removes the equivalence of the two oxygen atoms, resulting in an ester type of bond formation between the carboxylic acid group and the TiO_2 surface. On the basis of the IR data of adsorbed complexes, this type of coordination can be ruled out, leaving only two possibilities, chelation and/or unidentate bridging coordination. Recently Fennie et al. and other groups have used the differences between the asymmetric and symmetric bands in the ionic and the adsorbed states as criteria for identifying the carboxylate-anchoring mode.[36−39] If the difference between the carboxylate group asymmetric and symmetric bands in the adsorbed state is lower than that in the free state, then the anchoring mode is chelation. However, if the difference is greater than or equal to that in the ionic state, then the anchoring mode is unidentate bridging. The separation between the carboxylate group asymmetric and symmetric bands in the free (264 cm^{-1}) and the adsorbed states (263 cm^{-1}) suggests that the dye anchors with unidentate bridging coordination to the TiO_2. Recent theoretical studies on the interaction of formic acid and sodium formate on anatase (101) and ZnO (1010) surfaces showed that the formation of the bidentate chelation mode is highly unstable, leaving the possibility of a bridging coordination mode.[40,41] Our findings are in agreement with the theoretical studies of the interaction of formic acid on TiO_2.

Scheme 1

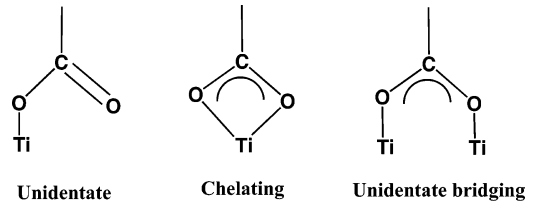

Electronic Spectra. The electronic absorption spectral data of complexes **5**−**8** measured in DMF solvent were included in Table 1. The absorption maxima are listed for the intense lowest-energy metal-to-ligand charge-transfer (MLCT) bands

(34) Nazeeruddin, M. K.; Zakeeruddin, S. M.; Humphry-Baker, R.; Gorelsky, S. I.; Lever, A. B. P.; Grätzel, M. *Coord. Chem. Rev.* **2000**, *208*, 213.
(35) Fillinger, A.; Parkinson, B. A. *J. Electrochem. Soc.* **1999**, *146*, 4559.
(36) Duffy, N. W.; Dobson, K. D.; Gordon, K. C.; Robinson, B. H.; McQuillan, A. *J. Chem. Phys. Lett.* **1977**, *266*, 451.
(37) Finnie, K. S.; Bartlett, J. R.; Woolfrey, J. L. *Langmuirr* **1998**, *14*, 2744.
(38) Deacon, G. B.; Phillips, R. *J. Coord. Chem. Rev.* **1989**, *33*, 227.
(39) Mehrotra, R. C.; Bohra, R. *Metal Carboxylates*; Academic Press: New York, 1983.
(40) Vittadini, A.; Selloni, A.; Rotzinger, F. P.; Grätzel, M. *J. Phys. Chem. B* **2000**, *104*, 1300.
(41) Persson, P.; Lunell, S.; Ojamae, L. *Int. J. Quantum Chem.* **2002**, *89*, 172.

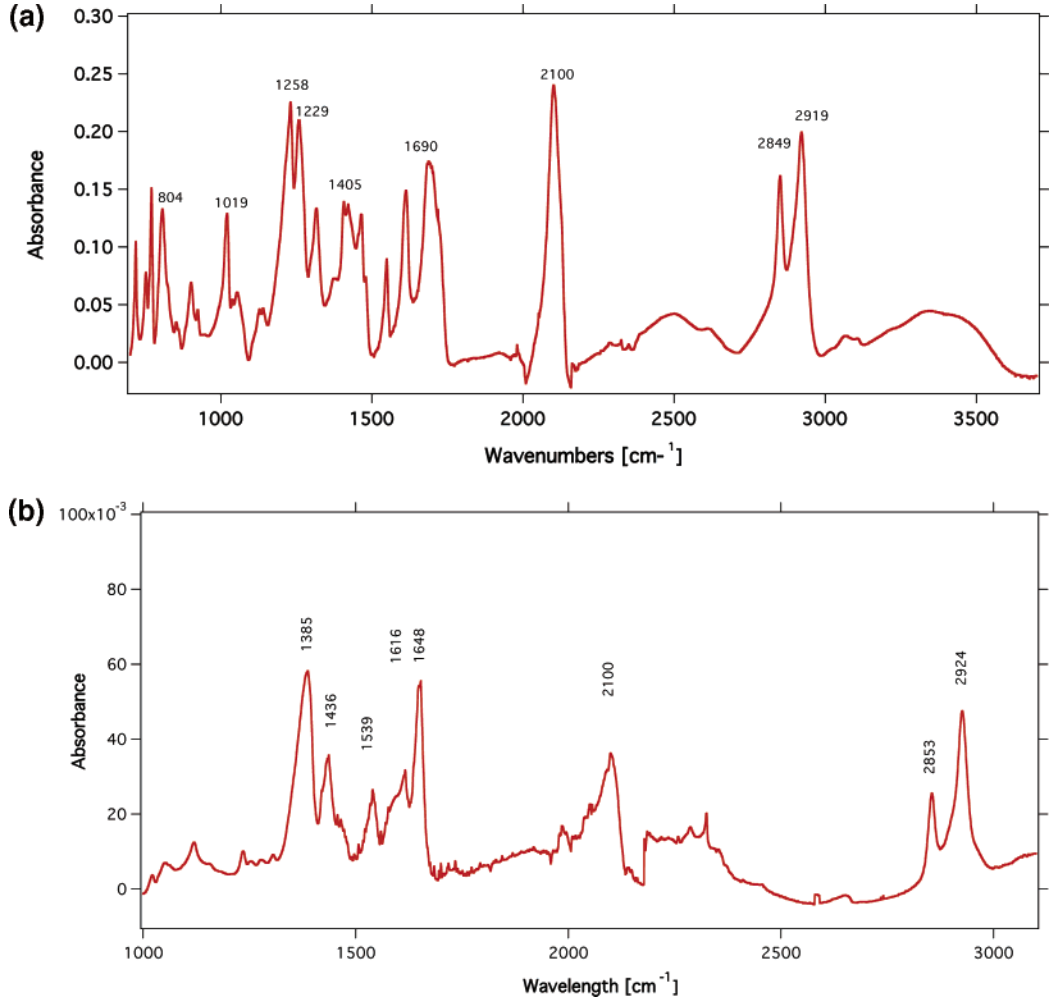

Figure 6. (a) ATR-FTIR spectra of complex **8**, obtained using a solid sample. (b) ATR-FTIR spectra of complex **8** adsorbed onto a 2 μm thick TiO_2 film.

in DMF. In general, the complexes **5**−**8** show broad and intense visible bands in the 370−550 nm region due to MLCT transitions.[42] Complex **5** in DMF solvent shows two broad visible bands at 537 and 392 nm that are assigned to MLCT origin. The band in the UV region at 313 nm is assigned to intra-ligand ($\pi-\pi^*$) charge-transfer transitions.[43] The complexes **6** and **7** in dichloromethane show maxima at 500 nm, and in ethanol at 520 nm due to the solvatochromic effect.

Deprotonation of the COOH groups in these complexes blue-shifts the $\pi-\pi^*$ charge-transfer band from 312 to 310 nm and the low-energy MLCT band from 534 to 514 nm (Figure 7a). The blue shift is due to an increase in the energy of the LUMO of the ligand, causing the $\pi-\pi^*$ and d$\pi-\pi^*$ transitions to occur at higher energies. However, the band at 294 nm in complex **8** due to 4,4′-bis(dodecan-12-ol)-2,2′-bipyridine $\pi-\pi^*$ charge-transfer transitions is unaffected in the pH range 2−10. The molar extinction coefficient of the lowest energy MLCT band in heteroleptic complexes **5**−**8** is lower (around 15%) compared to that of the *cis*-dithiocyanatobis(4,4′-dicarboxylic acid-2,2′-bipyridine)-ruthenium(II) complex. For comparison, the UV/vis spectral data of the homoleptic complex of *cis*-dithiocyanatobis(4,4′-dicarboxylic acid-2,2′-bipyridine)ruthenium(II) complex are included in Table 1.

The absorption spectra of complexes **5**−**8** anchored on a 6 μm thick TiO_2 nanocrystalline electrode from ethanol solution show the low-energy MLCT maximum at 538 nm, which is slightly red shifted compared to the solution spectra. This is due to the fact that, on the electrode, the carboxylate groups bind to the TiO_2 surface, in which Ti^{4+} acts as an electron acceptor that is stronger than a proton, which causes a slight decrease in the LUMO of dcbpy. Complexes **6** and **7** adsorb on a TiO_2 surface in lower quantities compared to complexes **5** and **8**. It is interesting to note that the amount of dye adsorbed on the 6 μm thick TiO_2 nanocrystalline electrode from dilute solutions (3×10^{-4} M in 1:1 acetonitrile and *tert*-butyl alcohol) over 24 h is comparable to the dye adsorbed from a 9×10^{-3} M solution in DMF over 30 min.

The emission maxima of complexes **5**−**8**, which were obtained at room temperature by excitation at 530 nm in DMF solution, are included in Table 1. Figure 7b shows representative absorption and emission spectra of complex **5**. The emission intensity of complex **8** is significantly lower, and the maxima are red-shifted compared to those of complexes **5**−**7**, which could be due to proton-induced

(42) Balzani, V.; Juris, A.; Venturi, M.; Campagna, S.; Serroni, S. *Chem. Rev.* **1996**, *96*, 759.
(43) Meyer, T. J. *Pure Appl. Chem.* **1986**, *50*, 1293.

Table 3. Comparison of Photocurrent, Open-Circuit Potential, Fill Factor, and the Efficiency Obtained Using Complexes **5**−**8** on 12 + 4 μm Thick TiO_2 Electrodes under AM 1.5 Sun[a]

complex	dye solution	electrolyte	IPCE (%)	current (mA/cm^2)	V_{oc} (mV)	*ff*	efficiency (η%)
5	DMF	1376	75	15.3	695	0.66	7.01
5	C_2H_5OH	1376	78	15.8	685	0.63	6.81
6	C_2H_5OH	1376	63	15.47	676	0.71	7.42
6	$CHCl_3$	1376	64	12.53	673	0.71	6.0
7	C_2H_5OH	1376	79	16.11	676	0.7	7.62
7	$CHCl_3$	1376	65	12.65	666	0.72	6.06
8	DMF	1376	86	17.13	673	0.72	8.30
8	1:1 C_2H_5OH/*t*-BuOH	1376	82	17.5	700	0.72	8.86

[a] The measurements were made using 1376 electrolyte whose composition is 0.6 M M-methyl-*N*-butyl imdiazolium iodide, 0.05 M iodine, 0.05 M LiI, and 0.5 M *tert*-butylpyridine in a 50:50 (v/v) mixture of valeronitrile and acetonitrile.

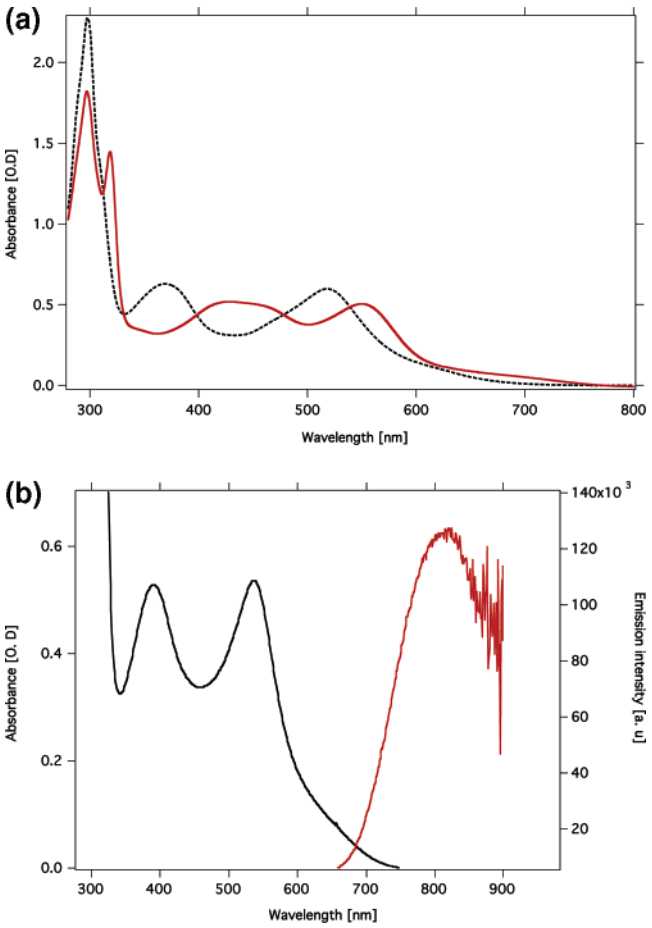

Figure 7. (a) UV/vis absorption spectrum of a 4.7 × 10^{-5} M solution of deprotonated (black dashed line) and protonated (red solid line) complex **8**, measured in DMF. (b) UV/vis absorption and emission spectra of a 4.5 × 10^{-5} M solution of complex **5** in DMF.

quenching of the excited state by the presence of −OH groups on the hydrophobic chains.[44]

Photovoltaic Performance. The TiO_2 electrodes were heated at 400 °C for 20 min before being dipped into the dye solution. The electrodes were left for 18−22 h in a dilute dye solution of 3 × 10^{-4} M in ethanol or 1:1 acetonitrile/*tert*-butyl alcohol. Alternatively, a measured volume of the concentrated dye solution, 9 × 10^{-3} M in DMF, was pipetted (10 μL for 0.5 cm^2 TiO_2 area) onto the surface of the TiO_2 electrode, and the dye solution was left for 10−30 min. The dye-coated electrodes were rinsed quickly with acetonitrile and used as such for photovoltaic measurements. The photovoltaic performance of cells dipped for 30 min in concentrated solution and of those dipped for 18 h in dilute solution is similar.

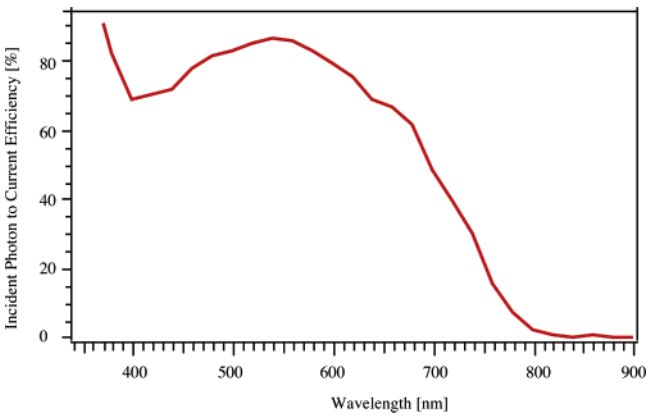

Figure 8. Photocurrent action spectrum, obtained with the complex **8** attached to nanocrystalline TiO_2 film. The incident photon-to-current conversion efficiency is plotted as a function of the wavelength of the exciting light. The electrolyte composition was 0.6 M M-methyl-*N*-butyl imdiazolium iodide, 0.05 M iodine, 0.05 M LiI, and 0.5 M *tert*-butylpyridine in a 50:50 (v/v) mixture of valeronitrile and acetonitrile.

The performance of **5**−**8** as sensitizers on nanocrystalline TiO_2 electrodes was studied using an electrolyte having a composition of 0.6 M M-methyl-*N*-butyl imdiazolium iodide, 0.05 M iodine, 0.05 M LiI, and 0.5 M *tert*-butylpyridine in a 50:50 (v/v) mixture of valeronitrile and acetonitrile. The photovoltaic data, such as current, open-circuit voltage, fill factor, and the efficiency of the complexes **5**−**8**, are collected in Table 3. The photocurrent action spectra obtained with the TiO_2 films coated with a monolayer of complex **8** in a sandwich cell under illumination by simulated AM 1.5 solar light are shown in Figure 8. The incident monochromatic photon-to-current conversion efficiency (IPCE) is plotted as a function of excitation wavelength, showing a plateau region at 87%. The photocurrent action spectra of the amphiphilic heteroleptic complexes show broad features covering a large part of the visible spectrum. From the overlap integral of this curve with the standard global AM 1.5 solar emission spectra, one measures a short-circuit photocurrent density of 16.5 mA/cm^2. In agreement with this measurement under standard global AM 1.5 solar conditions, the cell gave a photocurrent density of 17.5 mA/cm^2, an open-circuit

(44) Kalyanasundaram, K.; Nazeeruddin, M. K. *Chem. Phys. Lett.* **1992**, *193*, 292.

potential of 700 mV, and a fill factor of 0.72, yielding close to 8.8% efficiency.

Conclusions

In the present study, we have identified the dimeric $[Ru(Cl)_2(cymene)]_2$ complex as a very convenient and versatile precursor for the one-pot synthesis of amphiphilic heteroleptic complexes. The spectroscopic and electrochemical data revealed that, by engineering dyes at the molecular level, one could fine-tune solubility and electrochemical properties of sensitizers, which are useful for solar-cell applications. The ATR-FTIR data show that these dyes anchor to the TiO_2 surface using two carboxylic acid groups in a bridging-coordination mode. We have employed a swift self-assembling deposition procedure for amphiphilic complexes that yields close to 9% power conversion efficiency under AM 1.5 sun.

Acknowledgment. We acknowledge financial support of this work by the Swiss Federal Office for Energy (OFEN), the U.S. Air Force Research Office (Contract No. F61775-00-C0003), and NANOMAX (Contract No. ENK6-CT-2001-00575 of the fifth RTD framework program by EU and funded by OFES, Bern). We thank P. Comte and Dr. Marie Jirousek for their assistance and Dr. Robin Humphry-Baker for his time and helpful discussions.

IC049906M